

# MoReMouse: Monocular Reconstruction of Laboratory Mouse

Yuan Zhong\* Jingxiang Sun\* Liang An† Yebin Liu†  
Tsinghua University

{zhong-y19, anliang, liuyebin}@mails.tsinghua.edu.cn, starkjxsun@gmail.com

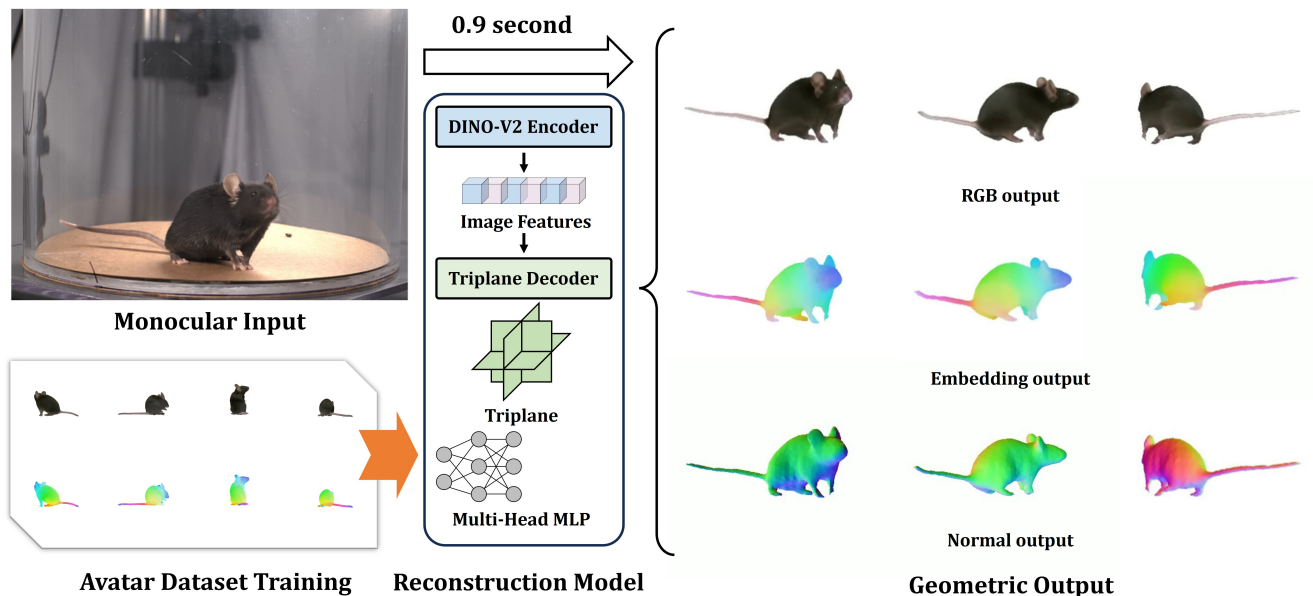


Figure 1. We present **MoReMouse**, the first monocular dense 3D reconstruction framework for laboratory mice. Given a single-view input (top-left, captured using an iPhone 15 Pro), MoReMouse predicts high-fidelity surface geometry and appearance using a transformer-based triplane architecture. The model is trained on a dataset constructed from real multi-view videos fitted to a Gaussian mouse avatar. Our method supports fast inference and outputs RGB renderings, semantic embeddings, and normal maps from a single image.

## Abstract

Laboratory mice play a crucial role in biomedical research, yet accurate 3D mouse surface motion reconstruction remains challenging due to their complex non-rigid geometric deformations and textureless appearance. Moreover, the absence of structured 3D datasets severely hinders the progress beyond sparse keypoint tracking. To narrow the gap, we present MoReMouse, the first monocular dense 3D reconstruction network tailored for laboratory mice. To achieve this goal, we highlight three key designs. First, we construct the first high-fidelity dense-view synthetic dataset for mice, by rendering our self-designed realistic Gaussian

mouse avatar. Second, MoReMouse adopts a transformer-based feedforward architecture with triplane representation, achieving high-quality 3D surface generation from a single image. Third, we create geodesic-based continuous correspondence embeddings on mouse surface, which serve as strong semantic priors to improve reconstruction stability and surface consistency. Extensive quantitative and qualitative experiments demonstrate that MoReMouse significantly outperforms existing open-source methods in accuracy and robustness. Video results are available at <https://zyyw-eric.github.io/MoreMouse-webpage/>.

\*Equal contribution.

†Corresponding author.

# 1. Introduction

Laboratory mice, as widely used model animals, are fundamental to disease modeling and neuroscience studies. Understanding their three-dimensional (3D) motion dynamics provides valuable insights for medical and life sciences [13].

Over the last decade, deep learning has revolutionized both 2D and 3D animal pose estimation, with methods such as DeepLabCut [24], SLEAP [29] and DANNCE [11] becoming standard tools across diverse species including mice. However, these methods are limited to sparse keypoint tracking and ignore important 3D surface motion. Although several papers have tried to build articulated mouse mesh models [1, 4, 6] and use them for mouse surface tracking [2, 17], they still face two key drawbacks. First, manually designed skinning weights are infeasible to represent the complex dynamic deformations of a mouse, resulting in severe self-penetration during its free movement. Second, existing mouse mesh fitting methods require heavy and sensitive multi-view optimization process, hindering its application for more convenient single view scenarios.

The rapid evolution of 3D generative AI has blurred the boundary between 3D reconstruction and 3D generation [39], where large scale 3D datasets such as Objaverse [9, 10] play a crucial role in this trend. Thanks to the datasets, Large Reconstruction Models (LRMs) [14, 38, 39] demonstrate single-view feedforward 3D reconstruction for general objects, significantly outperform traditional feedback approaches like DreamFusion [30] in both reconstruction quality and efficiency. Although LRMs have the potential to revolutionize monocular mouse reconstruction, they require ground truth 3D geometries or dense-view images for supervision, which is unavailable for laboratory mice. Additionally, mice exhibit highly dynamic non-rigid deformations, and their furry skins lack prominent visual features, making it more challenging to reconstruct surface motion of mice.

In this paper, we present **MoReMouse**, the first **monocular dense 3D reconstruction model for laboratory mouse**. MoReMouse is built upon transformer architectures and triplane representation, enabling efficient, feedforward 3D reconstruction. To compensate for the scarcity of dense-view 3D mouse dataset, we construct the first animatable Gaussian avatar of mouse using an articulated mouse model [6] and Gaussian Splatting [16]. Inspired by recent human avatar modeling [20], we propose a 2D UV-based intermediate mouse pose representation to drive Gaussian point clouds. Thanks for the free-view rendering ability and diverse pose space of the avatar, we build a synthetic 64-view dataset, enabling effective training of MoReMouse network.

Despite of the synthetic dataset, the framework of MoReMouse integrates multiple architectural and training enhancements inspired by LRMs. Specifically, we

employ a two-stage training strategy, initially pretraining the model with triplane-NeRF [7, 25] representations, followed by fine-tuning with triplane-DMTet[35] for higher-fidelity reconstructions. To further improve the stability and robustness of dense surface reconstruction, we introduce geodesic-based feature embeddings, which enhance semantic consistency of surfaces across frames. In experiments, we compare MoReMouse with existing open-sourced feedforward large reconstruction models such as TripoSR [39], Triplane-GS [50], InstantMesh [45] and LGM [38] on our synthetic dataset, proving the superiority of MoReMouse for monocular mouse reconstruction and novel view synthesis. Qualitative results on real-world videos captured by hand-held iPhone further confirm the generalization ability of MoReMouse (Fig. 1). As a whole, MoReMouse represents a crucial step toward high-fidelity, efficient 3D reconstruction of mouse, and will facilitate broader applications in biomedical research. To summarize, our key contributions include:

- We introduce MoReMouse, the first monocular dense 3D reconstruction model for laboratory mouse, surpassing existing open-source alternatives.
- We develop the first Gaussian avatar model for mice and generate a large scale dense-view synthetic mouse dataset for training and evaluation.
- We integrate geodesic-based continuous correspondence embeddings with feedforward 3D reconstruction, improving single-view reconstruction stability and quality.

## 2. Related work

### 2.1. 3D Representation of Mouse

Previously, most 3D mouse motion capture toolboxes reconstruct mouse 3D keypoints by algebraic triangulation [12, 15, 26, 27], voxel-based triangulation [11] or even by markers [22, 23]. However, 3D keypoints provide only sparse geometric structures, neglecting dense surface information which is essential to represent highly dynamic mouse body shapes or interpret social touch information [2, 17]. To represent the mouse surface, [5] proposes an articulated mesh model based on computed tomography scans. Although this model is useful for the motion capture of mouse surface from multiview videos [2], its manually designed skinning weight could not capture the realistic dynamic surface motion of a moving mouse. ArMo [4] presents a similar mouse mesh model, but lacks realistic geometric details. For the rat, which shares a shape similar to that of the mouse, researchers pay similar efforts to build articulated mesh model [1] yet face the same challenge. In this paper, we try to overcome the limitation of explicit articulated representation of mouse by reconstructing the implicit surface of it.

## 2.2. Monocular Reconstruction of Animals

Since the proposal of SMAL (Skinned Multi-Animal Linear) model which represents several quadrupedal species [52], predicting the pose and shape parameters of SMAL from images has dominated the monocular reconstruction of animals [3, 21, 32, 33, 44, 53, 54]. Although they have demonstrated satisfactory performance for species such as dogs, horses, cattle, and tigers, they cannot reconstruct rodents due to the limited shape space of SMAL. The AWOL model [51] further extends SMAL to represent rodents using CLIP [31] and supports monocular shape estimation. However, it still relies on a predefined articulated model, without the ability to express geometric deformation beyond linear blend skinning. Some recent papers try to build animal avatars from videos by augmenting the skinning weights or adding additional deformations. For example, BANMo [47] and RAC [48] build fully implicit cat and dog avatars using neural deformation field and differentiable rendering [25], Gart [18] and Animal Avatars [34] build dog avatars with SMAL geometric embedding and neural appearance. However, these methods all require a heavy optimization process during inference, and rely on dense pose estimation such as CSE [28] or SMAL parameters for initialization.

## 2.3. Large Reconstruction Model

Large reconstruction models have recently achieved substantial progress in generating high-quality 3D content [14, 19, 36, 37, 41, 46, 49, 50]. These models are typically trained in an end-to-end fashion to predict implicit 3D representations, often through triplane-based neural radiance fields. Some approaches operate from a single input image [14, 41, 46, 49, 50], while others use multi-view images generated by novel view synthesis techniques [19, 36]. Meanwhile, UNet-based architectures have also proven effective in generating multiplane or Gaussian representations [38, 42], providing alternative and efficient formats for 3D reconstruction.

However, these methods generally depend on access to 3D supervision, such as ground-truth shapes or high-quality multi-view data, during training. This reliance poses a significant challenge for in-the-wild applications, where diverse and scalable 3D datasets remain scarce compared to their 2D counterparts [8, 10, 43]. In addition, their reconstructions often exhibit limitations in geometric detail and texture quality, making them less suitable for scenarios that demand high visual fidelity.

## 3. Method

Our goal is to achieve dense geometry reconstruction of a mouse from a single viewpoint via a feed-forward 3D generative approach, where representation and supervision play

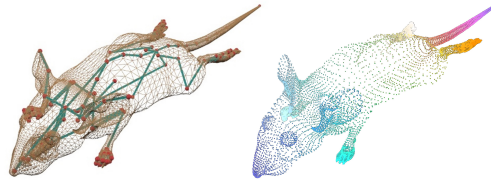


Figure 2. Visualization of the articulated mouse mesh and the learned geodesic embedding. Left: our mesh model consists of 140 articulated joints and 14,522 vertices, forming a kinematically consistent 3D structure for pose fitting. Right: color-coded visualization of the learned geodesic feature embedding, where principal components are mapped to HSV color space to enhance surface separability and promote reconstruction consistency.

crucial roles in ensuring high-quality generation.

To construct dataset for effective supervision (Sec. 3.1), we design the first Gaussian avatar for mouse (Sec. 3.1.2), which introduces an additional bias on top of the mesh model to better capture complex mouse surface deformations from videos (Sec. 3.1.3).

Our proposed MoReMouse model builds upon an LRM-like structure (Sec. 3.2) and exploits the strengths of both Triplane-NeRF for an initial coarse training phase and Triplane-DMTet for fine-grained training (Sec. 3.2.1). Furthermore, to enhance tracking stability and preserve surface consistency, we introduce a geodesic-distance-based feature embedding (Sec. 3.2.2). These embeddings serve as additional semantic priors, improving the robustness of dense reconstruction. The details of our training and optimization procedure are provided in (Sec. 3.2.3).

## 3.1. Synthetic Dataset using Gaussian Avatar

### 3.1.1. Mouse Parametric Model

As shown in Fig 2, we employ the established mouse mesh model used in [2] as avatar control signals. The model consists of  $K = 140$  articulated joints and 14,522 vertices, and conforms to Linear Blend Skinning (LBS) for pose control. The whole parameter set is denoted as  $\Psi$ , including joint rotations  $\theta \in \mathbb{R}^{3K}$ , global translation  $t \in \mathbb{R}^3$ , global rotation  $r \in \mathbb{R}^3$ , global scale  $s \in \mathbb{R}$  and bone length deformation parameters  $B \in \mathbb{R}^{21}$  (Please refer to [2] for more details). We decompose  $\Psi$  into local parameters  $\Psi_l = \{\theta, B\}$  and global parameters  $\Psi_g = \{r, t, s\}$  for the sake of simplicity.

### 3.1.2. Gaussian Mouse Avatar

Gaussian point clouds [16] use an explicit parameterization for 3D representation. Each Gaussian point is characterized by a mean position  $\mu \in \mathbb{R}^3$  and an anisotropic covariance matrix  $\Sigma$ :

$$G(x) = e^{-\frac{1}{2}(x-\mu)^T \Sigma^{-1}(x-\mu)}. \quad (1)$$

To facilitate optimization, the covariance matrix is reformulated as  $\Sigma = RSS^T R^T$ , where  $S$  is a diagonal scaling

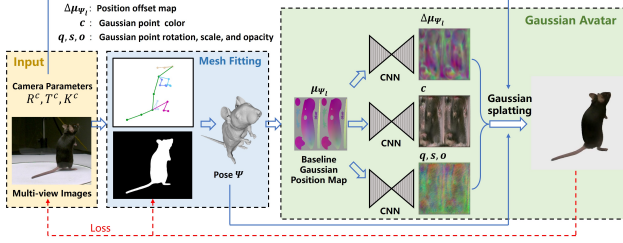


Figure 3. Pipeline of the Gaussian Mouse Avatar Generation. The process begins with Mesh Fitting, followed by Gaussian model training.

matrix controlled by a three-dimensional vector  $s \in \mathbb{R}^3$ , and the rotation matrix  $R$  is represented by a normalized quaternion  $q \in \mathbb{R}^4$ . Additionally, each Gaussian encodes a color  $c \in \mathbb{R}^3$  and an opacity  $o \in \mathbb{R}$ . During rendering, Gaussians within the pixel projection region are sorted by depth and composited using alpha blending.

Inspired by Animatable Gaussians [20], we employ texture-based deformation transfer to train a neural representation of the Gaussian point cloud avatar, incorporating bias correction beyond the skeletal model, as shown in Fig. 3. Our key idea is to parameterize the mouse UV texture, mapping each valid texel in the UV space to a corresponding Gaussian point, where the texture color represents the Gaussian’s position.

To obtain the canonical space representation, we set  $\Psi_g = 0$  and drive the mesh model using only  $\Psi_l$ , resulting in canonical vertex coordinates  $V_{\Psi_l}$ . The UV-mapped positions of these vertices are used to interpolate Gaussian locations in the UV texture via barycentric coordinates. This defines the baseline Gaussian position map  $\mu_{\Psi_l}$ :

$$\mu_{\Psi_l} = \mathcal{D}_{\Psi_l}(\mu_0), \quad (2)$$

where  $\mu_0$  is the UV coordinate map in the neutral pose, and  $\mathcal{D}_{\Psi_l}$  represents the LBS deformation mapping induced by the skeletal model.

During Gaussian optimization, we incorporate a CNN-based offset prediction module. A convolutional neural network StyleUNet [40] predicts the position offset map  $\Delta\mu_{\Psi_l}$ , conditioned on the UV coordinate map  $\mu_{\Psi_l}$ , to refine the Gaussian positions:

$$\mu'_{\Psi_l} = \mathcal{D}_{\Psi_l}(\mu_0 + \Delta\mu_{\Psi_l}). \quad (3)$$

The CNN also estimates additional Gaussian attributes, including color  $c_{\Psi_l}$ , opacity  $o_{\Psi_l}$ , covariance rotation parameters  $q_{\Psi_l}$ , and scaling parameters  $s_{\Psi_l}$ . Then the Gaussian Splatting rendering function generates the view-dependent rendered image  $I_c^{\text{rend}}$ :

$$I_c^{\text{rend}} = GS(R_c, T_c, K_c, \mu'_{\Psi_l}, c_{\Psi_l}, q'_{\Psi_l}, s_{\Psi_l}), \quad (4)$$

where  $GS(\cdot)$  denotes the Gaussian splatting renderer, and  $R_c, T_c, K_c$  are camera parameters.

### 3.1.3. Avatar Training

To train the Gaussian avatar, we define loss functions between the real image  $I_c$  and the rendered image  $I_c^{\text{rend}}$ :

$$\mathcal{L} = \mathcal{L}_1(I_c - I_c^{\text{rend}}) + \lambda_{\text{SSIM}}(1 - \mathcal{L}_{\text{SSIM}}(I_c, I_c^{\text{rend}})) + \lambda_{\text{LPIPS}}\mathcal{L}_{\text{LPIPS}}(I_c, I_c^{\text{rend}}), \quad (5)$$

where  $\mathcal{L}_{\text{SSIM}}$  quantifies structural similarity, while  $\mathcal{L}_{\text{LPIPS}}$  assesses perceptual similarity. The loss weights are set to  $\lambda_{\text{SSIM}} = 0.2$  and  $\lambda_{\text{LPIPS}} = 0.1$ . Additionally, we enforce Total Variation (TV) loss to regularize Gaussian point cloud smoothness.

We use a 6-view mouse video sequence ”markerless\_mouse\_1” proposed in [11] for avatar training. Each sequence captures 18,000 frames of a single freely moving mouse in an open field at 1152x1024@100FPS, where the mouse mesh models are provided by [2]. Note that, we only use 800 frames for training, which are uniformly sampled from the first 8000 frames of ”markerless\_mouse\_1”. Avatar training takes 400k steps.

## 3.2. MoReMouse Architecture

### 3.2.1. Transformer and Triplane Representation

Similar to LRM [14], MoReMouse adopts a Transformer and triplane-based architecture, designed for monocular 3D reconstruction. The model consists of three key components: an image encoder, an image-to-triplane decoder, and a triplane-based geometric representation that integrates both NeRF [25] and DMTet [35] for implicit and explicit geometry modeling.

First, the image encoder employs a pre-trained DINOv1 backbone to extract a latent feature vector from the input image. Then, a large Transformer decoder employs cross-attention to project these image features into a 3D triplane representation. This triplane-based geometric representation encodes color, density, and additional spatial attributes at any queried 3D location.

During the initial training phase, to regularize the convergence of the spatial density field, we do not introduce explicit geometry. Instead, we employ NeRF for differentiable volumetric rendering, allowing gradients to propagate throughout the entire space.

Once the density field has sufficiently converged, we introduce DMTet as an explicit geometric representation for further refinement. DMTet provides well-defined surfaces and enables direct geometric supervision.

The fine-scale structures of mice, particularly in the limbs and tail, present challenges for high-fidelity reconstruction in a feed-forward manner. To address this, we modify the LRM framework by increasing the triplane resolution to 64 to improve detail preservation. Additional architectural details are provided in the supplementary materials.

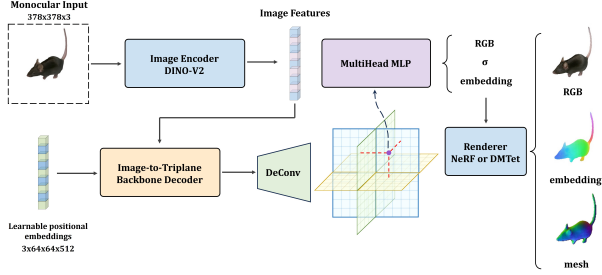


Figure 4. Architecture of the MoReMouse reconstruction network. Given a monocular input image, a DINO-V2 encoder extracts high-level image features, which are processed by a transformer-based decoder to generate a triplane representation. These triplanes, combined with learnable positional embeddings, are queried by a Multi-Head MLP to predict per-point color, density, and geodesic embedding. Rendering is performed via either NeRF (for volumetric supervision) or DMTet (for explicit geometry output), producing RGB images, color-coded embeddings, and surface meshes.

### 3.2.2. Feature Embedding for Surface Consistency

The reconstruction of mice poses significant challenges due to their black fur, which lacks distinctive surface features, and the presence of intricate fine-scale geometric details. Inspired by Animatable Gaussians [20], we incorporate feature embeddings into the mouse surface representation to enhance reconstruction stability. These embeddings serve as additional color channels during training, acting as supervisory signals for MoReMouse rendering.

Specifically, given the set of mouse model vertices  $V \in \mathbb{R}^{13059 \times 3}$ , we compute the pairwise geodesic distances between vertices to obtain the geodesic distance matrix:

$$G_V \in \mathbb{R}^{13059 \times 13059}, \quad G_V(i, j) = d_{\text{geo}}(V_i, V_j), \quad (6)$$

where  $d_{\text{geo}}(V_i, V_j)$  represents the geodesic distance between vertices  $V_i$  and  $V_j$ .

To learn a continuous correspondence embedding that captures the intrinsic structure of the mouse surface, we define the embedding matrix  $E \in \mathbb{R}^{13059 \times 3}$  and optimize it by minimizing the  $L_2$  loss between the embedding-derived distance matrix  $G_E$  and the geodesic distance matrix  $G_V$ :

$$\mathcal{L}_{\text{geo}} = \sum_{i,j} \|G_E(i, j) - G_V(i, j)\|_2^2, \quad (7)$$

where  $G_E(i, j) = \|E_i - E_j\|_2$  represents the Euclidean distance in the embedding space.

However, directly using these embeddings as color channels is suboptimal. The three-dimensional embeddings often form an elongated mouse-like shape in feature space, failing to fully utilize the available color space. Additionally, large dark or bright regions appear, lacking sufficient contrast against the black or white backgrounds used during

rendering. To address this, we perform Principal Component Analysis (PCA) on the embeddings, selecting the first two principal components as the hue (H) and saturation (S) values in the HSV color space, while keeping the value (V) channel fixed at 1:

$$H = \text{PCA}_1(E), \quad S = \text{PCA}_2(E), \quad V = 1. \quad (8)$$

This transformation improves the separability of the embeddings in the rendered images.

Notably, a simple rotation of the embeddings in color space can generate new feature mappings:

$$E' = R(\theta)E, \quad (9)$$

where  $R(\theta)$  is a rotation matrix. Extending the embeddings to higher dimensions could further improve reconstruction robustness. However, we leave the exploration of such extensions to future work.

### 3.2.3. Training and Optimization

Following the method outlined in Section 3.1.2, we generate freely renderable Mouse Avatars for each frame of the "markerless\_mouse\_1" video sequence. As the dataset consists of 18,000 frames, we use the first 6,000 frames for training and the last 6,000 frames for testing. To construct the training set, we sample two sets of 64 viewpoints per frame, rendering 12,000 multi-view scenes in total. The optical axes of these viewpoints converge at the scene origin.

During training, two randomly selected viewpoints from each scene serve as the input-output pair. To mitigate spatial ambiguity, we fix the mouse position at the scene origin. In preprocessing, we also apply translation and scaling transformations to the input images, ensuring that the mouse centroid is aligned with the image center and normalized to a consistent scale. Experimental results show that MoReMouse generalizes well from training on fixed perspectives to varying viewpoints in real-world scenarios.

We employ a two-stage training strategy, where NeRF-based volumetric rendering is first trained for 60 epochs to ensure proper density field convergence, followed by DMTet-based explicit geometry modeling for an additional 100 epochs to refine surface details.

The total training loss is defined as:

$$\mathcal{L} = \lambda_{\text{MSE}} \mathcal{L}_{\text{MSE}} + \lambda_{\text{depth}} \mathcal{L}_{\text{depth}} + \lambda_{\text{smoothL1}} \mathcal{L}_{\text{smoothL1}} + \lambda_{\text{mask}} \mathcal{L}_{\text{mask}} + \lambda_{\text{LPIPS}} \mathcal{L}_{\text{LPIPS}}. \quad (10)$$

Here,  $\mathcal{L}_{\text{MSE}}$  enforces pixel-wise supervision for both RGB values and feature embeddings, while  $\mathcal{L}_{\text{depth}}$  ensures depth consistency within the valid object region. The smooth L1 loss  $\mathcal{L}_{\text{smoothL1}}$  penalizes large RGB discrepancies, and  $\mathcal{L}_{\text{mask}}$  applies binary cross-entropy supervision to the predicted opacity maps. The perceptual loss  $\mathcal{L}_{\text{LPIPS}}$  measures high-level perceptual similarity in a deep feature space. The hyperparameters  $\lambda$  control the relative importance of each term.

## 4. Experiments

### 4.1. Experimental Setup

We evaluate MoReMouse on two types of testing datasets: a synthetic benchmark and a real-world captured dataset.

**Synthetic Evaluation Data.** We use the last 6,000 frames from the `markerless_mouse_1` sequence to generate a synthetic multi-view dataset consisting of 4 orthogonal viewpoints. These views are rendered using our Gaussian avatar pipeline and serve as a controlled evaluation set where ground-truth camera parameters and rendering conditions are known.

**Real Captured Data.** To assess performance under realistic conditions, we collect a real-world multi-view dataset using industrial cameras. This dataset contains 5,400 frames of freely moving mice captured from four calibrated viewpoints. The camera rotation angles relative to the reference view are  $0^\circ$ ,  $-33.39^\circ$ ,  $-78.60^\circ$ , and  $-181.02^\circ$ , respectively.

**Baselines.** Due to the lack of monocular 3D reconstruction methods specifically designed for mice, we compare MoReMouse against four general-purpose single-view reconstruction baselines:

- **TripoSR** [39]: A state-of-the-art open-source Large Reconstruction Model (LRM) known for strong single-view 3D generation performance.
- **Triplane-GS** [50]: A LRM variant based on Gaussian representations.
- **LGM** [38]: A multi-view diffusion-based method that reconstructs 3D Gaussian point clouds.
- **InstantMesh** [45]: A mesh-based 3D reconstruction method using multi-view diffusion priors.

For synthetic data, we additionally evaluate the multi-view diffusion baselines (LGM and InstantMesh) using ground-truth views as input, which serves as an approximate upper bound for multi-view reconstruction.

**Evaluation Protocol.** All methods are evaluated on the task of novel view synthesis, since obtaining ground-truth 3D geometry for mouse subjects is impractical. For each frame, a single view is used as input, and the remaining three views are used to evaluate the visual fidelity of synthesized images. We report three standard image-based metrics: Peak Signal-to-Noise Ratio (PSNR), Structural Similarity Index (SSIM), and Learned Perceptual Image Patch Similarity (LPIPS).

### 4.2. Experimental Results

**Quantitative Results.** We report the evaluation results on the synthetic and real-world datasets in Table 1. For each metric, we highlight the top-3 performing methods using color shading, with darker tones indicating better performance.

Table 1. Quantitative results on both synthetic and real-world datasets. MoReMouse achieves the best performance across all metrics in both domains, significantly outperforming baseline methods in terms of reconstruction fidelity.

Dataset	Method	PSNR $\uparrow$	SSIM $\uparrow$	LPIPS $\downarrow$
synthetic	<b>Ours</b>	22.027	0.9660	0.05279
	TripoSR	13.673	0.8032	0.18255
	Triplane-GS	18.049	0.9268	0.10151
	LGM	14.460	0.8805	0.13274
	InstantMesh	15.821	0.8987	0.11312
real	<b>Ours</b>	18.422	0.9478	0.08674
	TripoSR	11.518	0.8114	0.19672
	Triplane-GS	16.789	0.9298	0.11002
	LGM	15.215	0.9197	0.12838
	InstantMesh	15.631	0.9175	0.11339

Across all three metrics for novel view synthesis, MoReMouse consistently outperforms the baseline methods, demonstrating its ability to effectively infer plausible mouse geometry and pose from a single image. Notably, in Table 2, MoReMouse uses only a single input view, while LGM and InstantMesh are evaluated with 4 and 6 views respectively. For LGM, the 4 input views happen to coincide with the 4 evaluation viewpoints, offering an idealized setting that may favor the method. Nonetheless, MoReMouse achieves comparable performance despite relying on significantly less input information, underscoring its strong generalization capabilities in monocular reconstruction scenarios.

We also observe that the quantitative metrics on the real-world dataset are generally lower than on the synthetic dataset, especially for PSNR. This is largely due to the camera-mouse configuration: in the real dataset, the cameras are fixed while the mouse moves, whereas MoReMouse and all baselines assume that the mouse is centered and aligned across input-output views. This mismatch introduces pixel-level alignment errors, reducing PSNR. However, the perceptual metrics SSIM and LPIPS remain high, indicating that MoReMouse still reconstructs plausible and correct mouse poses and shapes. This confirms that models trained on synthetic data can generalize to real-world mouse motion capture scenarios.

Table 2. Comparison with multi-view diffusion-based methods using ground-truth viewpoints on the synthetic dataset. Despite using only a single view, MoReMouse performs competitively with multi-view approaches that use 4 or 6 calibrated inputs.

Method	PSNR $\uparrow$	SSIM $\uparrow$	LPIPS $\downarrow$
Ours (single view)	22.027	0.9660	0.05279
LGM (4 views)	23.998	0.9698	0.06458
InstantMesh (6 views)	28.295	0.9831	0.02716

**Qualitative Results.** To visually compare MoReMouse with baseline methods, we select three representative frames from both the synthetic and real-world sequences. As shown in Fig. 5 and Fig. 6, MoReMouse generates mice with coherent appearance and physically plausible postures, accurately capturing tail and limb movements. These results remain stable even though each frame is inferred independently, showing smooth motion continuity.

In contrast, baseline methods often exhibit structural distortions in novel views and inconsistent pose transitions across frames. Diffusion-based approaches such as InstantMesh and LGM tend to produce view-inconsistent geometry, likely due to the absence of strong priors on mouse anatomy. Single-view approaches like Triplane-GS and TripoSR frequently fail to reconstruct accurate poses, especially under extreme articulations or occlusions.

### 4.3. Ablation Study

#### 4.3.1. Comparison with Finetuned TripoSR

In previous experiments, we compared MoReMouse with four general-purpose single-view 3D reconstruction baselines, demonstrating the effectiveness of our complete training pipeline. However, these reconstruction models were pre-trained on datasets that may not contain sufficient small animal or mouse-like samples, which could limit their performance on our mouse-specific benchmarks.

To assess whether the improvements of MoReMouse are due to architectural and representation innovations rather than only data augmentation, we fine-tune TripoSR on our mouse dataset using a similar training protocol. Specifically, we train the model for 120 epochs with a learning rate of  $1 \times 10^{-6}$ . As shown in Table 3 and illustrated in Fig. 7, the fine-tuned TripoSR achieves improved performance compared to its original version, but still lags behind MoReMouse across most metrics. This suggests that our model architecture, including the triplane encoding and geodesic feature embedding, plays a critical role in achieving high-fidelity reconstructions.

#### 4.3.2. Effect of Feature Embedding

We evaluate the effectiveness of the geodesic feature embedding module by training a variant of MoReMouse with-

Table 3. Comparison between MoReMouse and TripoSR fine-tuned on mouse data.

Dataset	Method	PSNR $\uparrow$	SSIM $\uparrow$	LPIPS $\downarrow$
<i>synthetic</i>	Ours	22.027	0.9660	0.05279
	TripoSR-Tuned	21.996	0.9676	0.06333
<i>real</i>	Ours	18.422	0.9478	0.08674
	TripoSR-Tuned	18.162	0.9461	0.09354

out this component. As shown in Table 4 and visualized in Fig. 8, removing the embedding leads to noticeably degraded reconstruction quality, particularly around fine-scale structures.

Without embedding supervision, the model struggles to maintain surface consistency in anatomically delicate regions such as limbs and tails. As evident in the first, third, and fourth rows of Fig. 8, the full model produces sharper and more accurate reconstructions of the paws and extremities. In the second row, the embedded model also better preserves subtle texture details around the snout. These observations support our design choice to use surface-based semantic priors. The geodesic embedding encourages coherent geometry and finer detail recovery.

Table 4. Ablation study on the effect of feature embedding. Removing embedding results in lower reconstruction quality, especially in perceptual similarity.

Dataset	Method	PSNR $\uparrow$	SSIM $\uparrow$	LPIPS $\downarrow$
<i>synthetic</i>	full model	22.027	0.9660	0.05279
	w/o embedding	21.805	0.9655	0.05467
<i>real</i>	full model	18.422	0.9478	0.08674
	w/o embedding	18.250	0.9469	0.08767

### 4.4. Failure cases

Figure 9 showcases typical failure cases on real-world data. The first row highlights the model’s inability to generalize to rare upright postures, due to the absence of such poses in the training set. This leads to implausible geometry and emphasizes the need for more pose-diverse avatar data.

In the second row, reconstruction fails when the tail occludes the head—especially under shaved-fur conditions—causing the model to misinterpret head structure. While our preprocessing removes background, we do not explicitly account for occlusions from scene objects or self-occlusion, which can degrade reconstruction fidelity.

Additionally, we observe that small regions such as feet and snouts are more prone to distortion, likely due to lim-

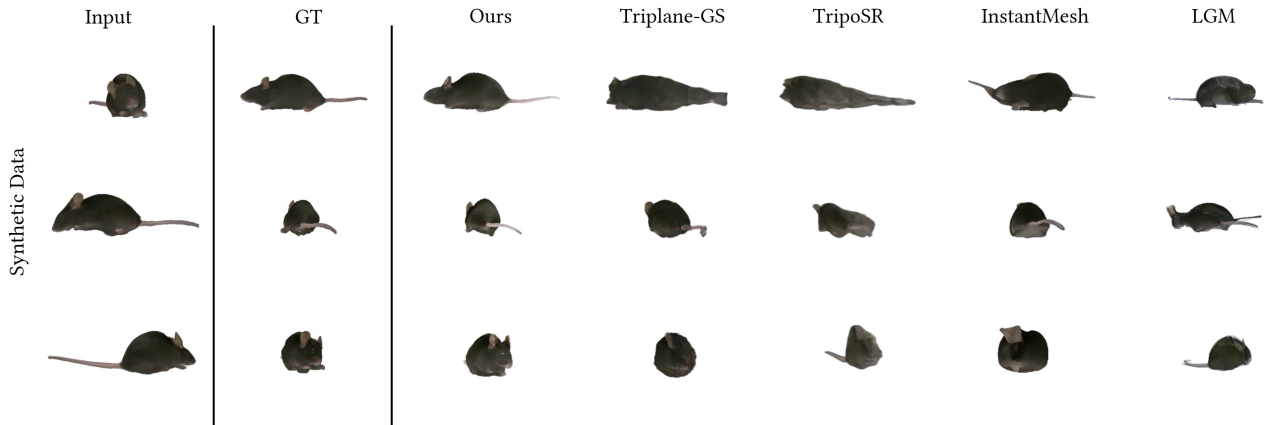


Figure 5. Qualitative comparison of novel view synthesis results on synthetic data. MoReMouse produces coherent and anatomically plausible reconstructions, accurately capturing mouse posture and geometry, while baseline methods often exhibit structural distortions.

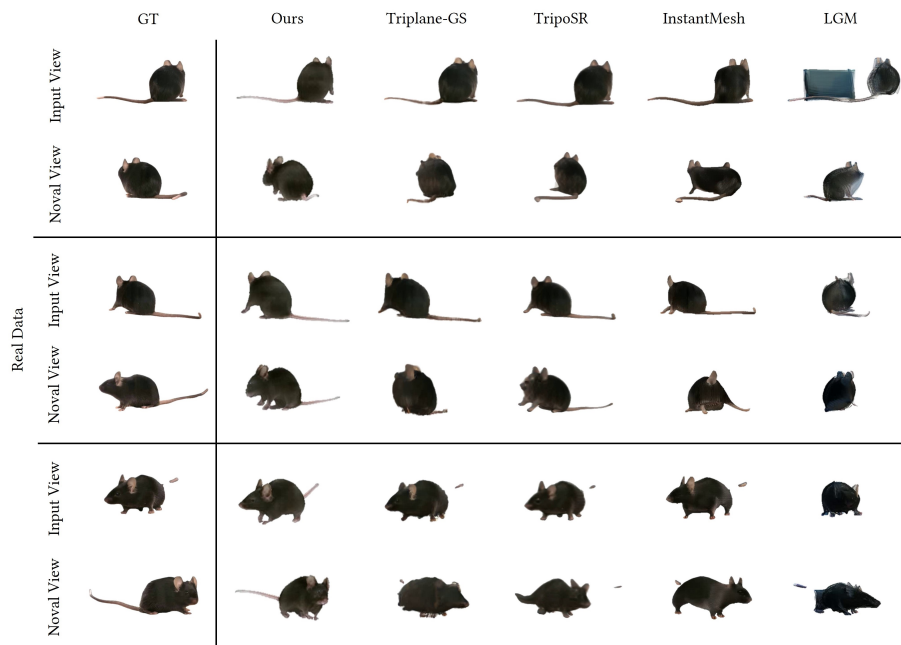


Figure 6. Qualitative comparison of novel view synthesis results on real data. MoReMouse generalizes well to real-world mouse recordings, maintaining consistent geometry and appearance across views, while baseline methods often suffer from inconsistent shapes and misaligned postures.

ited resolution in those areas. Future work may explore resolution-aware refinement or occlusion-robust modeling to address these limitations.

## 5. Discussion

**Summary** In this paper, we present **MoReMouse**, the first monocular dense 3D reconstruction model tailored for laboratory mice. Unlike existing single-view 3D methods designed for general objects or humans, MoReMouse addresses the unique challenges posed by small animals, in-

cluding non-rigid deformation, low surface texture, and limited training data. Our approach integrates transformer-based triplane representations, a Gaussian avatar modeling pipeline, and geodesic surface feature embeddings to achieve robust and high-fidelity reconstructions from a single image. We demonstrate strong performance across both synthetic and real datasets, outperforming state-of-the-art reconstruction baselines in terms of visual quality and perceptual consistency. Ablation studies further validate the architectural contributions of our model beyond dataset-specific priors. We hope that MoReMouse can serve as a

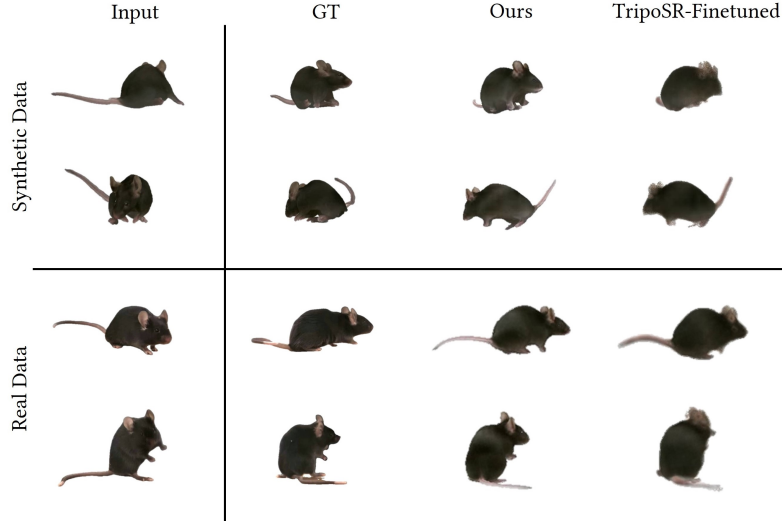


Figure 7. Qualitative comparison between our MoReMouse method and a finetuned TripoSR baseline. MoReMouse produces sharper and more anatomically coherent results. In contrast, TripoSR—based on volumetric NeRF rendering—tends to generate blurry boundaries and over-smoothed geometry, especially around fine structures like the ears.

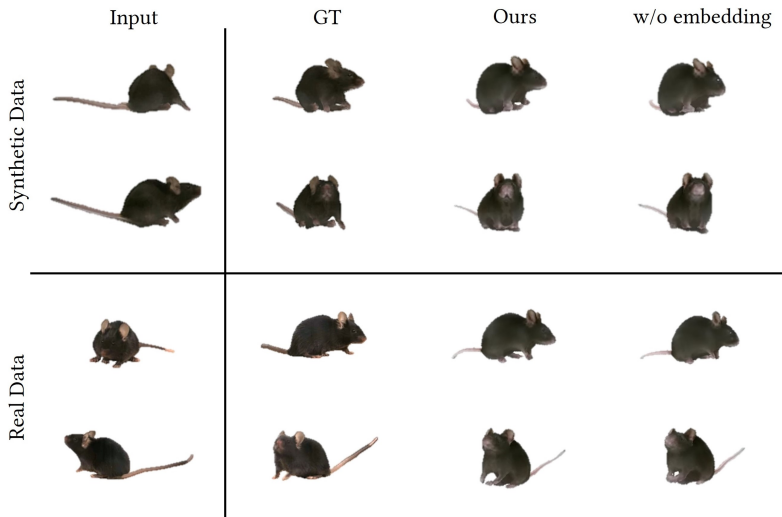


Figure 8. Qualitative comparison with and without geodesic feature embedding. The full model produces sharper and more consistent geometry, especially around limbs (rows 1, 3, 4) and snout texture (row 2). Embeddings help guide fine-grained surface details and improve anatomical accuracy.

foundation for future research in computational ethology and non-rigid animal modeling, promoting more precise, efficient, and scalable behavioral analysis tools for biomedical research.

**Limitations.** While MoReMouse offers a promising solution to monocular mouse reconstruction, several limitations remain that warrant future investigation. (1) *Limited training diversity.* Our training data is derived from a single video sequence of a single mouse under consistent lighting

and appearance. This limits the generalization of the model to other mice with varying fur color, size, or under different lighting conditions. (2) *Pose tracking in global coordinates.* The current system assumes that the mouse is always centered in a canonical scene space. This design limits our ability to track full 3D poses in a real-world coordinate system.

**Ethical Statement.** All procedures involving mice in this study were non-invasive and observational, involving

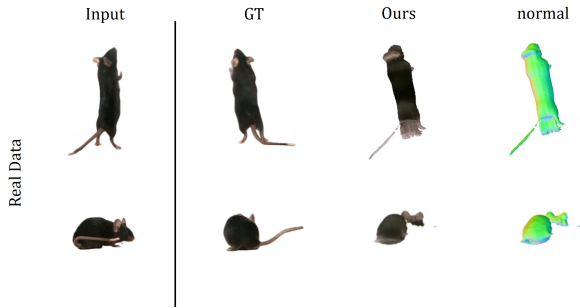


Figure 9. Representative failure cases. Top: failure due to lack of standing mouse data in training, leading to unrealistic reconstructions. Bottom: failure due to tail-induced occlusion from shaved fur, which interferes with head feature extraction.

only video recording of natural behaviors without any physical intervention or stress to the animals. The experiments were conducted in accordance with internationally recognized guidelines for laboratory animal care. Since the study involved only observational methods, ethical approval was not required by the relevant institutional animal care and local ethics authority. The mice were housed under standard conditions in compliance with local animal welfare regulations, and all efforts were made to minimize disturbance during filming. The study adhered to the 3Rs principle (Replacement, Reduction, Refinement) in animal research.

## Acknowledgements

This work was supported by the National Natural Science Foundation of China (No. 62125107) and the Shuimu Tsinghua Scholar Program (2024SM324).

## References

- [1] Diego Aldarondo, Josh Merel, Jesse D Marshall, Leonard Hasenclever, Ugne Klibaite, Amanda Gellis, Yuval Tassa, Greg Wayne, Matthew Botvinick, and Bence P Ólveczky. A virtual rodent predicts the structure of neural activity across behaviours. *Nature*, 632(8025):594–602, 2024. 2
- [2] Liang An, Jilong Ren, Tao Yu, Tang Hai, Yichang Jia, and Yebin Liu. Three-dimensional surface motion capture of multiple freely moving pigs using mammal. *Nature Communications*, 14(1):7727, 2023. 2, 3, 4
- [3] Benjamin Biggs, Oliver Boyne, James Charles, Andrew Fitzgibbon, and Roberto Cipolla. Who left the dogs out?: 3D animal reconstruction with expectation maximization in the loop. In *ECCV*, 2020. 3
- [4] James P Bohoslav, Mohammed Abdal Monium Osman, Akshay Jaggi, Sofia Soares, Caleb Weinreb, Sandeep Robert Datta, and Christopher D Harvey. Armo: An articulated mesh approach for mouse 3d reconstruction. *bioRxiv*, pages 2023–02, 2023. 2
- [5] Luis A Bolaños, Dongsheng Xiao, Nancy L Ford, Jeff M LeDue, Pankaj K Gupta, Carlos Doebeli, Hao Hu, Helge Rhodin, and Timothy H Murphy. A three-dimensional virtual mouse generates synthetic training data for behavioral analysis. *Nature Methods*, 18(4):378–381, 2021. 2
- [6] Luis A Bolaños, Dongsheng Xiao, Nancy L Ford, Jeff M LeDue, Pankaj K Gupta, Carlos Doebeli, Hao Hu, Helge Rhodin, and Timothy H Murphy. A three-dimensional virtual mouse generates synthetic training data for behavioral analysis. *Nature methods*, 18(4):378–381, 2021. 2
- [7] Eric R Chan, Connor Z Lin, Matthew A Chan, Koki Nagano, Boxiao Pan, Shalini De Mello, Orazio Gallo, Leonidas J Guibas, Jonathan Tremblay, Sameh Khamis, et al. Efficient geometry-aware 3d generative adversarial networks. In *Proceedings of the IEEE/CVF Conference on Computer Vision and Pattern Recognition*, pages 16123–16133, 2022. 2
- [8] Angel X Chang, Thomas Funkhouser, Leonidas Guibas, Pat Hanrahan, Qixing Huang, Zimo Li, Silvio Savarese, Manolis Savva, Shuran Song, Hao Su, et al. Shapenet: An information-rich 3d model repository. *arXiv preprint arXiv:1512.03012*, 2015. 3
- [9] Matt Deitke, Ruoshi Liu, Matthew Wallingford, Huong Ngo, Oscar Michel, Aditya Kusupati, Alan Fan, Christian Laforte, Vikram Voleti, Samir Yitzhak Gadre, et al. Objaverse-xl: A universe of 10m+ 3d objects. *Advances in Neural Information Processing Systems*, 36:35799–35813, 2023. 2
- [10] Matt Deitke, Dustin Schwenk, Jordi Salvador, Luca Weihs, Oscar Michel, Eli VanderBilt, Ludwig Schmidt, Kiana Ehsani, Aniruddha Kembhavi, and Ali Farhadi. Objaverse: A universe of annotated 3d objects. In *Proceedings of the IEEE/CVF conference on computer vision and pattern recognition*, pages 13142–13153, 2023. 2, 3
- [11] Timothy W Dunn, Jesse D Marshall, Kyle S Severson, Diego E Aldarondo, David GC Hildebrand, Selmaan N Chettih, William L Wang, Amanda J Gellis, David E Carlson, Dmitriy Aronov, et al. Geometric deep learning enables 3d kinematic profiling across species and environments. *Nature methods*, 18(5):564–573, 2021. 2, 4
- [12] Yaning Han, Ke Chen, Yunke Wang, Wenhao Liu, Zhouwei Wang, Xiaojing Wang, Chuanliang Han, Jiahui Liao, Kang Huang, Shengyuan Cai, et al. Multi-animal 3d social pose estimation, identification and behaviour embedding with a few-shot learning framework. *Nature Machine Intelligence*, pages 1–14, 2024. 2
- [13] DL Hickman, J Johnson, Tracy H Vemulapalli, JR Crisler, and R Shepherd. Commonly used animal models. *Principles of animal research for graduate and undergraduate students*, page 117, 2016. 2
- [14] Yicong Hong, Kai Zhang, Jiuxiang Gu, Sai Bi, Yang Zhou, Difan Liu, Feng Liu, Kalyan Sunkavalli, Trung Bui, and Hao Tan. Lrm: Large reconstruction model for single image to 3d. *arXiv preprint arXiv:2311.04400*, 2023. 2, 3, 4
- [15] Pierre Karashchuk, Katie L Rupp, Evyn S Dickinson, Sarah Walling-Bell, Elischa Sanders, Eiman Azim, Bingni W Brunton, and John C Tuthill. Anipose: a toolkit for robust markerless 3d pose estimation. *Cell Reports*, 36(13), 2021. 2
- [16] Bernhard Kerbl, Georgios Kopanas, Thomas Leimkühler, and George Drettakis. 3d gaussian splatting for real-time radiance field rendering. *TOG*, 42(4):1–14, 2023. 2, 3

- [17] Ugne Klibaite, Tianqing Li, Diego Aldarondo, Jumana F Akoad, Bence P Ölveczky, and Timothy W Dunn. Mapping the landscape of social behavior. *Cell*, 188(8):2249–2266, 2025. 2
- [18] Jiahui Lei, Yufu Wang, Georgios Pavlakos, Lingjie Liu, and Kostas Daniilidis. Gart: Gaussian articulated template models. In *Proceedings of the IEEE/CVF conference on computer vision and pattern recognition*, pages 19876–19887, 2024. 3
- [19] Jiahao Li, Hao Tan, Kai Zhang, Zexiang Xu, Fujun Luan, Yinghao Xu, Yicong Hong, Kalyan Sunkavalli, Greg Shakhnarovich, and Sai Bi. Instant3d: Fast text-to-3d with sparse-view generation and large reconstruction model. *ArXiv*, abs/2311.06214, 2023. 3
- [20] Zhe Li, Zerong Zheng, Lizhen Wang, and Yebin Liu. Animatable gaussians: Learning pose-dependent gaussian maps for high-fidelity human avatar modeling. In *Proceedings of the IEEE/CVF conference on computer vision and pattern recognition*, pages 19711–19722, 2024. 2, 4, 5
- [21] Jin Lyu, Tianyi Zhu, Yi Gu, Li Lin, Pujin Cheng, Yebin Liu, Xiaoying Tang, and Liang An. Animer: Animal pose and shape estimation using family aware transformer, 2024. 3
- [22] Jesse D Marshall, Diego E Aldarondo, Timothy W Dunn, William L Wang, Gordon J Berman, and Bence P Ölveczky. Continuous whole-body 3d kinematic recordings across the rodent behavioral repertoire. *Neuron*, 109(3):420–437, 2021. 2
- [23] Jesse D Marshall, Ugne Klibaite, Amanda Gellis, Diego E Aldarondo, Bence P Ölveczky, and Timothy W Dunn. The pair-r24m dataset for multi-animal 3d pose estimation. *bioRxiv*, pages 2021–11, 2021. 2
- [24] Alexander Mathis, Pranav Mamidanna, Kevin M Cury, Taiga Abe, Venkatesh N Murthy, Mackenzie Weygandt Mathis, and Matthias Bethge. Deeplabcut: markerless pose estimation of user-defined body parts with deep learning. *Nature neuroscience*, 21(9):1281–1289, 2018. 2
- [25] Ben Mildenhall, Pratul P Srinivasan, Matthew Tancik, Jonathan T Barron, Ravi Ramamoorthi, and Ren Ng. Nerf: Representing scenes as neural radiance fields for view synthesis. *Communications of the ACM*, 65(1):99–106, 2021. 2, 3, 4
- [26] Arne Monsees, Kay-Michael Voit, Damian J Wallace, Juergen Sawinski, Edyta Charyasz, Klaus Scheffler, Jakob H Macke, and Jason ND Kerr. Estimation of skeletal kinematics in freely moving rodents. *Nature Methods*, 19(11):1500–1509, 2022. 2
- [27] Tanmay Nath, Alexander Mathis, An Chi Chen, Amir Patel, Matthias Bethge, and Mackenzie Weygandt Mathis. Using deeplabcut for 3d markerless pose estimation across species and behaviors. *Nature Protocols*, 14(7):2152–2176, 2019. 2
- [28] Natalia Neverova, David Novotny, Marc Szafraniec, Vasil Khalidov, Patrick Labatut, and Andrea Vedaldi. Continuous surface embeddings. *Advances in Neural Information Processing Systems*, 33:17258–17270, 2020. 3
- [29] Talmo D Pereira, Nathaniel Tabris, Arie Matsliah, David M Turner, Junyu Li, Shruthi Ravindranath, Eleni S Papadoyannis, Edna Normand, David S Deutsch, Z Yan Wang, et al. Sleap: A deep learning system for multi-animal pose tracking. *Nature methods*, 19(4):486–495, 2022. 2
- [30] Ben Poole, Ajay Jain, Jonathan T Barron, and Ben Mildenhall. Dreamfusion: Text-to-3d using 2d diffusion. *arXiv preprint arXiv:2209.14988*, 2022. 2
- [31] Alec Radford, Jong Wook Kim, Chris Hallacy, Aditya Ramesh, Gabriel Goh, Sandhini Agarwal, Girish Sastry, Amanda Askell, Pamela Mishkin, Jack Clark, et al. Learning transferable visual models from natural language supervision. In *International conference on machine learning*, pages 8748–8763. PMLR, 2021. 3
- [32] Nadine Rueegg, Silvia Zuffi, Konrad Schindler, and Michael J Black. Barc: Learning to regress 3d dog shape from images by exploiting breed information. In *Proceedings of the IEEE/CVF Conference on Computer Vision and Pattern Recognition*, pages 3876–3884, 2022. 3
- [33] Nadine Rüegg, Shashank Tripathi, Konrad Schindler, Michael J Black, and Silvia Zuffi. Bite: Beyond priors for improved three-d dog pose estimation. In *Proceedings of the IEEE/CVF Conference on Computer Vision and Pattern Recognition*, pages 8867–8876, 2023. 3
- [34] Remy Sabathier, Niloy Jyoti Mitra, and David Novotny. Animal avatars: Reconstructing animatable 3D animals from casual videos. *ArXiv*, abs/2403.17103, 2024. 3
- [35] Tianchang Shen, Jun Gao, Kangxue Yin, Ming-Yu Liu, and Sanja Fidler. Deep marching tetrahedra: a hybrid representation for high-resolution 3d shape synthesis. *Advances in Neural Information Processing Systems*, 34:6087–6101, 2021. 2, 4
- [36] Yawar Siddiqui, Tom Monnier, Filippos Kokkinos, Mahendra Kariya, Yanir Kleiman, Emilien Garreau, Oran Gafni, Natalia V. Neverova, Andrea Vedaldi, Roman Shapovalov, and David Novotny. Meta 3d assetgen: Text-to-mesh generation with high-quality geometry, texture, and pbr materials. 2024. 3
- [37] Jingxiang Sun, Cheng Peng, Ruizhi Shao, Yuan-Chen Guo, Xiaochen Zhao, Yangguang Li, Yanpei Cao, Bo Zhang, and Yebin Liu. Dreamcraft3d++: Efficient hierarchical 3d generation with multi-plane reconstruction model. *arXiv preprint arXiv:2410.12928*, 2024. 3
- [38] Jiayang Tang, Zhaoxi Chen, Xiaokang Chen, Tengfei Wang, Gang Zeng, and Ziwei Liu. Lgm: Large multi-view gaussian model for high-resolution 3d content creation. In *European Conference on Computer Vision*, pages 1–18. Springer, 2024. 2, 3, 6
- [39] Dmitry Tochilkin, David Pankratz, Zexiang Liu, Zixuan Huang, Adam Letts, Yangguang Li, Ding Liang, Christian Laforte, Varun Jampani, and Yan-Pei Cao. Tripopr: Fast 3d object reconstruction from a single image. *arXiv preprint arXiv:2403.02151*, 2024. 2, 6
- [40] Lizhen Wang, Xiaochen Zhao, Jingxiang Sun, Yuxiang Zhang, Hongwen Zhang, Tao Yu, and Yebin Liu. Styleavatar: Real-time photo-realistic portrait avatar from a single video. In *ACM SIGGRAPH 2023 Conference Proceedings*, pages 1–10, 2023. 4
- [41] Peng Wang, Hao Tan, Sai Bi, Yinghao Xu, Fujun Luan, Kalyan Sunkavalli, Wenping Wang, Zexiang Xu, and Kai

- Zhang. Pf-lrm: Pose-free large reconstruction model for joint pose and shape prediction. 2023. 3
- [42] Zhengyi Wang, Yikai Wang, Yifei Chen, Chendong Xiang, Shuo Chen, Dajiang Yu, Chongxuan Li, Hang Su, and Jun Zhu. Crm: Single image to 3d textured mesh with convolutional reconstruction model. *ArXiv*, abs/2403.05034, 2024. 3
- [43] Tong Wu, Jiarui Zhang, Xiao Fu, Yuxin Wang, Jiawei Ren, Liang Pan, Wayne Wu, Lei Yang, Jiaqi Wang, Chen Qian, et al. Omniobject3d: Large-vocabulary 3d object dataset for realistic perception, reconstruction and generation. In *Proceedings of the IEEE/CVF Conference on Computer Vision and Pattern Recognition*, pages 803–814, 2023. 3
- [44] Jiacong Xu, Yi Zhang, Jiawei Peng, Wufei Ma, Artur Jesslen, Pengliang Ji, Qixin Hu, Jiehua Zhang, Qihao Liu, Jiahao Wang, et al. Animal3d: A comprehensive dataset of 3d animal pose and shape. In *Proceedings of the IEEE/CVF International Conference on Computer Vision*, pages 9099–9109, 2023. 3
- [45] Jiale Xu, Weihao Cheng, Yiming Gao, Xintao Wang, Shenghua Gao, and Ying Shan. Instantmesh: Efficient 3d mesh generation from a single image with sparse-view large reconstruction models. *arXiv preprint arXiv:2404.07191*, 2024. 2, 6
- [46] Yinghao Xu, Hao Tan, Fujun Luan, Sai Bi, Peng Wang, Jiahao Li, Zifan Shi, Kalyan Sunkavalli, Gordon Wetzstein, Zexiang Xu, and Kai Zhang. Dmv3d: Denoising multi-view diffusion using 3d large reconstruction model. *ArXiv*, abs/2311.09217, 2023. 3
- [47] Gengshan Yang, Minh Vo, Natalia Neverova, Deva Ramanan, Andrea Vedaldi, and Hanbyul Joo. Banmo: Building animatable 3d neural models from many casual videos. In *Proceedings of the IEEE/CVF Conference on Computer Vision and Pattern Recognition*, pages 2863–2873, 2022. 3
- [48] Gengshan Yang, Chaoyang Wang, N Dinesh Reddy, and Deva Ramanan. Reconstructing animatable categories from videos. In *Proceedings of the IEEE/CVF Conference on Computer Vision and Pattern Recognition*, pages 16995–17005, 2023. 3
- [49] Kai Zhang, Sai Bi, Hao Tan, Yuanbo Xiangli, Nanxuan Zhao, Kalyan Sunkavalli, and Zexiang Xu. Gs-lrm: Large reconstruction model for 3d gaussian splatting. *arXiv*, 2024. 3
- [50] Zi-Xin Zou, Zhipeng Yu, Yuan-Chen Guo, Yangguang Li, Ding Liang, Yan-Pei Cao, and Song-Hai Zhang. Triplane meets gaussian splatting: Fast and generalizable single-view 3d reconstruction with transformers. In *Proceedings of the IEEE/CVF conference on computer vision and pattern recognition*, pages 10324–10335, 2024. 2, 3, 6
- [51] Silvia Zuffi and Michael J Black. Awol: Analysis without synthesis using language. In *European Conference on Computer Vision*, pages 1–19. Springer, 2024. 3
- [52] Silvia Zuffi, Angjoo Kanazawa, David W Jacobs, and Michael J Black. 3d menagerie: Modeling the 3d shape and pose of animals. In *Proceedings of the IEEE Conference on Computer Vision and Pattern Recognition*, pages 6365–6373, 2017. 3
- [53] Silvia Zuffi, Angjoo Kanazawa, and Michael J Black. Lions and tigers and bears: Capturing non-rigid, 3d, articulated shape from images. In *Proceedings of the IEEE conference on Computer Vision and Pattern Recognition*, pages 3955–3963, 2018. 3
- [54] Silvia Zuffi, Angjoo Kanazawa, Tanya Berger-Wolf, and Michael J Black. Three-d safari: Learning to estimate zebra pose, shape, and texture from images” in the wild”. In *Proceedings of the IEEE/CVF International Conference on Computer Vision*, pages 5359–5368, 2019. 3

# MoReMouse: Monocular Reconstruction of Laboratory Mouse

## Supplementary Material

### 1. MoReMouse Model Details

We summarize the architectural and training hyperparameters of the MoReMouse model in Table 5, covering key components such as the image encoder, triplane representation modules, multi-head MLP, NeRF and DMTet renderers, and training configurations.

Table 5. MoReMouse Architecture and Training Hyperparameters

Module	Parameter	Value
Image Tokenizer	Type	dinov2-base
	Image resolution	$378 \times 378$
	Feature channels	768
Triplane Tokenizer	Plane size	$64 \times 64$
	Channels	512
Backbone	Input channels	512
	Attention layers	12
	Attention heads	16
	Attention head dimension	64
	Cross attention dimension	768
Triplane Upsampler	Input channels	512
	Output channels	80
	Output shape	$3 \times 80 \times 128 \times 128$
MultiHeadMLP	Neurons	64
	Shared hidden layers	10
	Hidden layers for density/feature/deformation heads	1
Renderer-NeRF	Samples per ray	128
	Radius	0.87
	Density activation	<code>trunc_exp</code>
	Density bias	-1.0
Renderer-DMTet	SDF bias	-4.0
	Isosurface resolution	$256^3$
Training	Learning rate	$1e-5$
	Optimizer	AdamW
	LR scheduler	CosineAnnealingLR
	Warm-up steps	3000
	$\lambda_{\text{mse}}, \lambda_{\text{LPIPS}}$	1.0
	$\lambda_{\text{mask}}$	0.3
	$\lambda_{\text{smooth}}, \lambda_{\text{depth}}$	0.2